Electrochimica Acta 471 (2023) 143366

Contents lists available at ScienceDirect

Electrochimica Acta

journal homepage: www.journals.elsevier.com/electrochimica-acta

CdSe-nanoparticles-regulated synthesis of ZnCo-MOFs derived conductive porous carbon nanoflakes on carbon cloth for flexible sodium-ion supercapacitors

Hanxue Zhao [a], Mai Li [a,*], Jintao Du [a], Yuhang Lei [a], Ayesha Irfan [a], Muhammad Imran [a], Chunrui Wang [a], Jun He [b], Zhongyi Sun [b], Paul K. Chu [c]

[a] College of Science, Donghua University, Shanghai 201620, China
[b] Semiconductor New Materials Research and Development Center, Shanghai Q-Tech Ltd., Zhengxue Road, Yangpu District, Shanghai, China
[c] Department of Physics, Department of Materials Science and Engineering, Department of Biomedical Engineering, City University of Hong Kong, Tat Chee Avenue, Kowloon, Hong Kong, China

ARTICLE INFO

Keywords:
Flexible electrode
Cadmium selenide
Porous carbon
Sodium-ion supercapacitor
Density-functional theory

ABSTRACT

Porous carbon derived from metal-organic frameworks (MOFs) represents a novel class of carbonaceous materials with unique structural characteristics, conductivity, and chemical stability, rendering them suitable for electrodes in supercapacitors. Herein, a three-dimensional structure of conductive porous carbon nanoflakes (CPCN) is synthesized based on MOFs composed of organic ligands containing zinc and cobalt. Nanoscale CdSe particles serving as energy-storage materials are incorporated into CPCN (CdSe/CPCN@CC) to form the flexible electrode for sodium-ion supercapacitors. The electrochemical properties of CdSe/CC, CdSe/ZnCo-MOF@CC, Cd/CPCN@CC, and CdSe/CPCN@CC are studied in 1 M Na_2SO_4. The CdSe/CPCN@CC electrode shows an impressive specific capacitance of 893.52 F g^{-1} at a current density of 0.125 mA cm^{-2} and excellent cycling stability with 80.68% retention after 10,000 cycles in 1.0 M Na_2SO_4. The asymmetric supercapacitor constructed with CdSe/CPCN@CC and 1 M $NaPF_6$ electrolyte shows a capacitance of 97.8 F g^{-1}, an energy density of 139.10 Wh kg^{-1}, and a power density of 589.82 W kg^{-1} at a current density of 1 mA cm^{-2}. In addition, the capacitance retention is 88.45% after 10,000 cycles. The electrochemical properties of CdSe/CPCN@CC are improved due to the incorporation of more active materials as well as the synergistic effects of the CdSe nanoparticles and CPCN. Density-functional theory (DFT) calculations reveal a sodium ion adsorption energy of -1.0692 eV and large DOS near the Fermi level. More importantly, in spite of severe mechanical bending, the device continues to power an LED array boding well for flexible and wearable applications.

1. Introduction

Due to the rapid development of portable electronic devices and electric vehicles, energy storage devices must meet the increasing demand by low-cost, large-scale, and high-efficiency applications [1,2]. In particular, supercapacitors (SCs) have garnered considerable attention due to their favorable charging-discharging characteristics, cycling stability, high power density, and environmental sustainability [3–5]. Supercapacitors can be classified into three types based on the energy storage mechanisms: electric double-layer capacitors (EDLCs), pseudocapacitors, and hybrid supercapacitors [6]. EDLCs store the energy by the formation of an electrical double layer at the electrode-electrolyte interface, while pseudocapacitors store the energy *via* fast, reversible Faradaic redox reactions at or near the electrode surface [7–9]. Hybrid supercapacitors combine the EDLC and pseudocapacitive storage mechanisms to deliver high energy and power densities [10,11]. The mechanisms suggest that the quality of pseudocapacitance is a critical factor in the fabrication of high-capacity supercapacitors, which serve as a bridge between EDLCs and hybrid supercapacitor systems [12].

Pseudocapacitance arises primarily from surface Faradaic reactions in which both the active materials and structure of the electrode play important roles [13]. Among the various pseudocapacitive materials, carbonaceous materials, conducting polymers, and transition metal compounds are common electrode materials in electrochemical energy

---

* Corresponding author.
E-mail address: limai@dhu.edu.cn (M. Li).

https://doi.org/10.1016/j.electacta.2023.143366
Received 18 July 2023; Received in revised form 15 October 2023; Accepted 15 October 2023

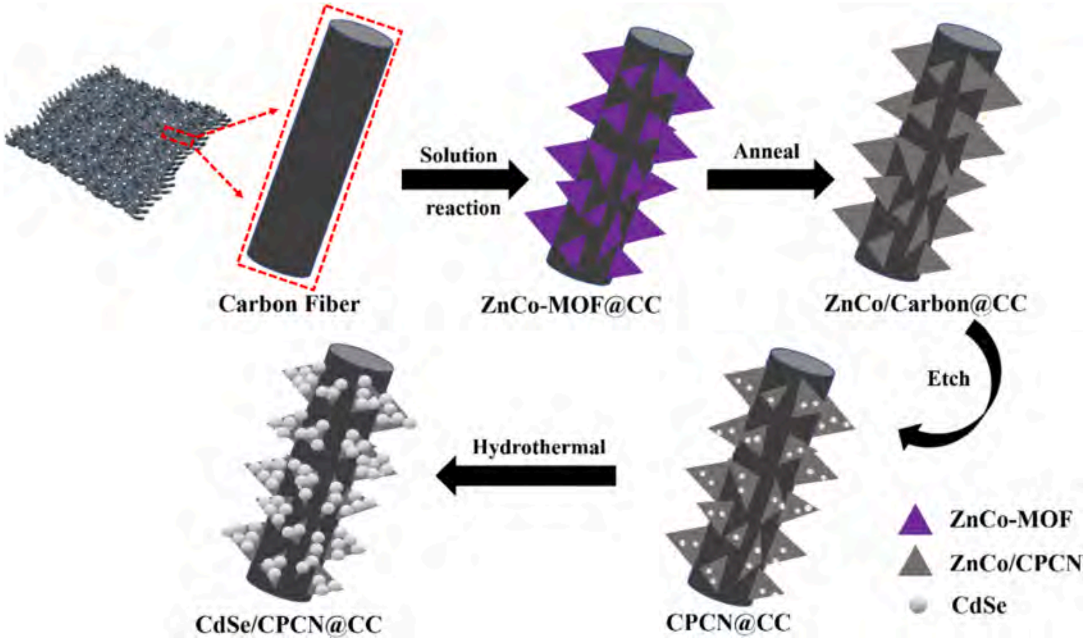

Fig. 1. Schematic illustration of the fabrication of the electrodes.

storage systems [14–17]. Transition metal selenides such as $MoSe_2$, $GeSe_2$, $NiSe_2$, $CoSe_2$, and CdSe have attracted much attention recently due to their excellent electrochemical properties and unique nanostructures [12,18–20]. Compounds prepared by combining selenium with transition metals can increase the activation energy of elemental selenium, reduce the activation voltage during charging, and improve the stability and lifespan of the electrode [21,22]. Besides, transition metal selenides possess merits such as high electrical conductivity, earth abundance, and easy fabrication [12,23]. The specific capacity of Al_2Se_3 nanorods prepared on reduced graphene oxide (rGO) nanosheets by Safdar et al. [24] is 1,138.1 F g^{-1}, and snow-crystal-like NiSe fabricated by Bekhit et al. using a binder-free and one-step solvothermal approach shows a high specific capacity of 763.5 F g^{-1} and initial specific capacity retention of 83% after 3,000 cycles [25]. Since the structure and morphology of Se-based compounds directly impact the specific capacitance, rate capability, cycling life, and safety, the selection of the appropriate materials and synthesis of the optimal Se-based compounds are critical for supercapacitor electrodes [26].

Cadmium possesses a relatively high theoretical specific capacitance of 546 mAh g^{-1}, and the stable voltage platform between reduction and oxidation enables reversible and efficient charging-discharging at fast charge-transfer rates in conjunction with good conductivity [12,27–29]. Cadmium sulfide (CdS) microspheres synthesized by Rathinamala et al. using an affordable and energy-saving approach show a specific capacitance of 854 F g^{-1}. The asymmetric supercapacitor composed of AC//CdS [30] shows an energy density of 8.4 W h kg^{-1} and a power density of 7.56 kW kg^{-1} at a current density of 20 A g^{-1}. Therefore, Combining Cd and Se elements as the CdSe can fully leverage the advantages of both elements, enhancing the electrochemical performance of electrode materials. Furthermore, combining carbonaceous materials with CdSe can improve the electrical conductivity, mechanical strength, and stability of energy storage materials and the cycling life and energy density of electrodes. For example, the conductive porous carbon nanoflakes (CPCN) derived from metal-organic frameworks (MOFs) are expected to be efficient electrodes [31,32].

As MOFs are prepared from organic ligands and metal ions, they have self-assembled and customizable structures that provide significant specific surface area [33,5] and have become intermediate templates or precursors for CPCN production [34–36]. In this work, by incorporating both cobalt and zinc metals, ZnCo-MOFs are deposited uniformly on the carbon cloth (CC) to form the ZnCo-MOFs@CC electrode with a large surface area [37,38]. The MOFs are carbonized under high-temperature inert conditions and then selectively etched to create the porous structure of CPNC@CC [39–41]. The CdSe nanoparticles are deposited on CPCN hydrothermally to form CdSe/CNCP@CC, as shown in Fig. 1. The electrochemical properties are determined in 1 M Na_2SO_4 and confirmed by density-functional theory (DFT) calculations. In order to demonstrate the practical feasibility, an asymmetric supercapacitor (ASCs) comprising CdSe/CPCN@CC as the negative electrode, carbon cloth coated with activated carbon (AC@CC) as the positive electrode, and 1 M $NaPF_6$ as the electrolyte is constructed and demonstrated for the 3.2 V window.

2. Materials and methods

2.1. Synthesis of ZnCo-MOF on carbon cloth (CC)

0.388 g of $Co(NO_3)_2{\cdot}6H_2O$ and 0.1983 g of $Zn(NO_3)_2{\cdot}6H_2O$ were dissolved in 40 mL of deionized (DI) water, and then 2-methylimidazole (1.3 g) in 40 mL of DI water was poured slowly into the solution and stirred magnetically at room temperature. A cleaned carbon cloth was immersed in the solution for 3 h at room temperature, washed several times with DI and ethanol, and dried overnight at 60 °C to obtain the ZnCo-MOF@CC precursor. The precursor was then annealed under N_2 at 700 °C at a rate of two degrees per minute and then kept for 2 h. After cooling to room temperature, the annealed ZnCo-MOF@CC is hydrothermally treated in 6 M HNO_3 at 90 °C for 24 h to remove Co^{2+}, Zn^{2+}, and by-products to obtain CPCN@CC.

2.2. Preparation of the composite electrode

A solution of 2 mmol $CdCl_2{\cdot}6H_2O$ in 50 mL of deionized (DI) water was prepared, and 2 mmol selenium powder was dissolved in 42 mL of the ethylenediamine solution and stirred. The two solutions were mixed and stirred for 15 min and then 14 ml of hydrazine hydrate was added dropwise. The mixture was transferred to a Teflon-lined stainless-steel autoclave containing CPCN@CC, sealed, and heated to 180 °C for about 6 h. After the reaction, the autoclave was cooled to room temperature naturally. The product was washed several times with DI and ethanol and dried at 60°C in air to form CdSe/CPCN@CC. For comparison, the

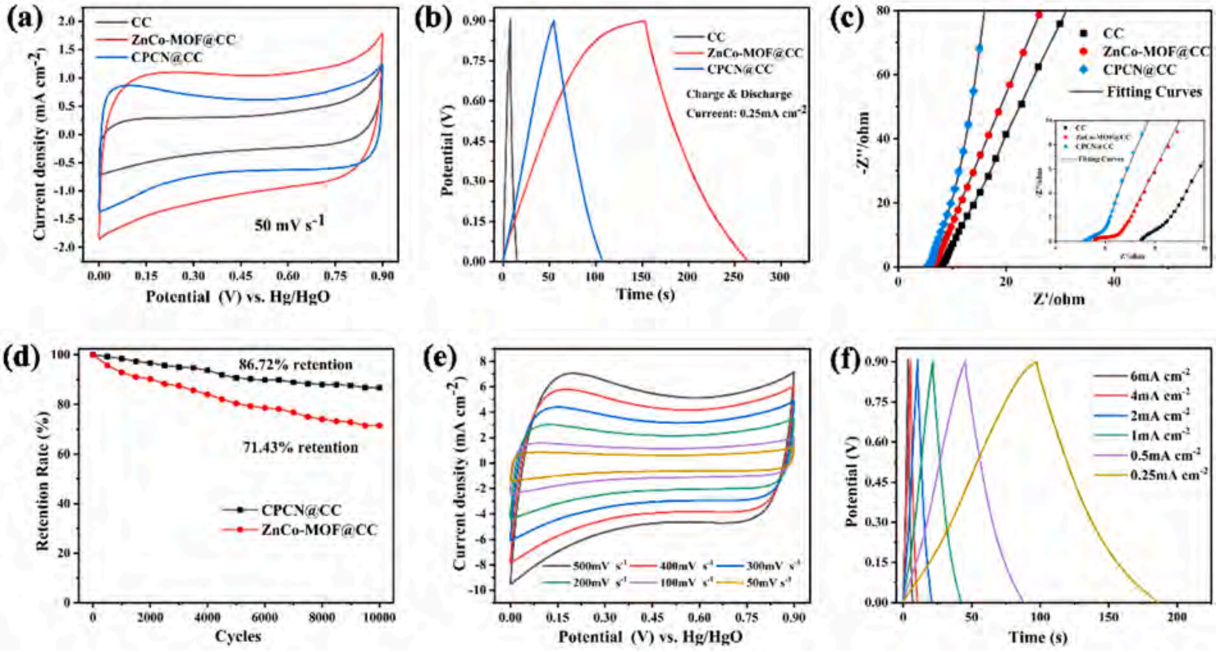

Fig. 2. (a) CV curves, (b) GCD curves and (c) Nyquist plots curves of CC, ZnCo-MOF@CC, and CPCN@CC; (d) Cycling stability of ZnCo-MOF@CC and CPCN@CC; (e) CV curves and (f) GCD curves of CPCN@CC.

Cd/CPCN@CC electrode was fabricated by the same method but without selenium powder. The remaining steps for the preparation of the CdSe/CPCN@CC electrode were the same.

2.3. Materials characterization

The morphology of the materials were characterized by field-emission scanning electron microscopy (FE-SEM, Hitachi, S-4800, Japan) and the elemental composition was determined by energy dispersive X-ray spectroscopy (EDS). The structure was analyzed by X-ray diffraction (XRD, Rigaku, RINT2000, Japan) and the elemental composition and chemical states were determined by X-ray photoelectron spectroscopy (XPS, Kratoms Axis Ultra DLD). The transmission electron micrographs (TEM) were acquired on the JEOL (JEM-2000 FX) at 200 kV. The content of carbon in prepared material was obtained by thermogravimetric analysis (TGA) in oxygen from 50 to 800°C. The Galvanostatic Intermittent Titration Technique (GITT) profile of CdSe/CPCN@CC was obtained by applying a series of current pulses at 0.15 mA g^{-1} for 20 min followed by a 1 h relaxation process.

2.4. Electrochemical measurements

The CHI660E electrochemical workstation was utilized to conduct the three-electrode assessment in 1 M Na_2SO_4. In this study, six working electrodes were tested for comparison, including CdSe/CPCN@CC, Cd/CPCN@CC, CPCN@CC, ZnCo-MOF@CC, CdSe/CC, and CC. The reference and counter electrodes were the saturated calomel electrode and platinum wire, respectively. The electrochemical properties were determined by cyclic voltammetry (CV), charging-discharging analysis (GCD), and electrochemical impedance spectroscopy (EIS). The composite electrodes were used as the positive electrode, while the negative electrode was fabricated by casting a slurry consisting of 80 wt% activated carbon, 10 wt% acetylene black, and 10 wt% Poly tetra fluoroethylene (PTFE) onto a nickel foam substrate, followed by drying at 80 °C. Both the positive and negative electrodes were cut into pieces with a diameter of 12 mm and then combined with the electrolyte and separator to form the supercapacitor. The electrolyte was 1 M $NaPF_6$ with the EC: PC ratio of 1:1 (vol%) with 5.0% FEC and the CR2032 coin-type cells were assembled to investigate the sodium storage properties using the CHI660E electrochemical workstation. The cells were assembled in a glove box (Mikrouna Super 1220/750/900, China) filled with argon, and the concentrations of O_2 and H_2O in the glovebox were below 0.1 ppm. All the electrochemical tests were performed at room temperature.

2.5. Computation

Density-functional theory (DFT) calculations were performed to elucidate the Na^+ storage mechanism. According to the experimental results, a model was constructed for growing Cd and CdSe on the porous carbon substrate (Fig. S1). First-principles calculations [42,43] were performed based on the spin-polarization density-functional theory (DFT) within the generalized gradient approximation (GGA) using the Perdew-Burke-Ernzerhof (PBE) [44] formulation. The projected augmented wave (PAW) potentials [45,46] described the ionic cores and took valence electrons into account using a plane wave basis set with a kinetic energy cutoff of 520 eV. Partial occupancies of the Kohn-Sham orbitals were allowed using the Gaussian smearing method with a width of 0.05 eV. The electronic energy was considered self-consistent when the energy change was smaller than 10^{-5} eV, and geometric optimization was considered convergent when the energy change was smaller than 0.05 eV $Å^{-1}$. The adsorption energies (Eads) were calculated as follows:

$$E_{\mathrm{ads}} = E_{\mathrm{ad/sub}} - E_{\mathrm{ad}} - E_{\mathrm{sub}}, \tag{1}$$

where $E_{\mathrm{ad/sub}}$, E_{ad}, and E_{sub} are the total energies of the optimized adsorbate/substrate system, adsorbate in the gas phase, and clean substrate, respectively.

3. Results and discussion

Fig. 1 depicts the schematic of the synthesis of CdSe/CPCN@CC, and the ZnCo-MOF precursor is prepared by the sol-gel method as shown in Fig. 1. The precursor is annealed and etched to form stable porous nanosheets of CPCN@CC. The color changes from purple-blue to black after annealing indicating uniform deposition of ZnCo-MOF on CC, and the black color confirms complete carbonization of the MOF forming

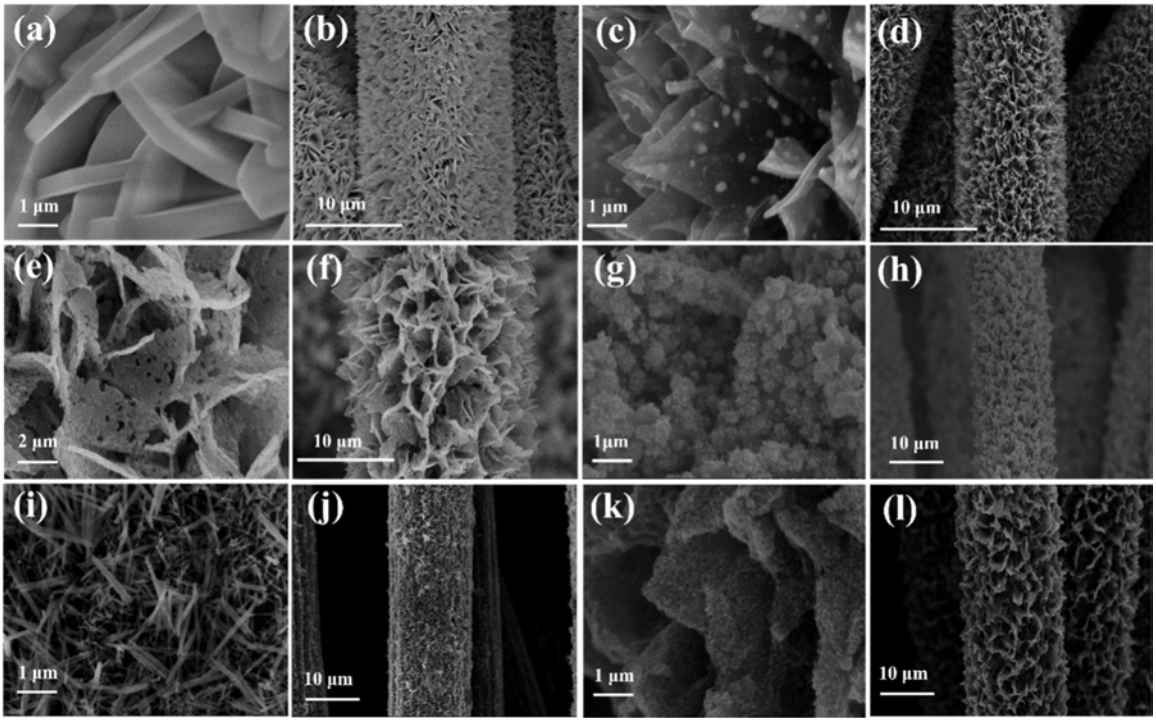

Fig. 3. SEM images of (a,b) ZnCo-MOF, (c,d) ZnCo-MOF after annealing, (e,f) ZnCo-MOF after atching (CPCN@CC), (g,h) CdSe/CPCN@CC, (i,j) Cd/CC, (k,l) Cd/CPCN@CC.

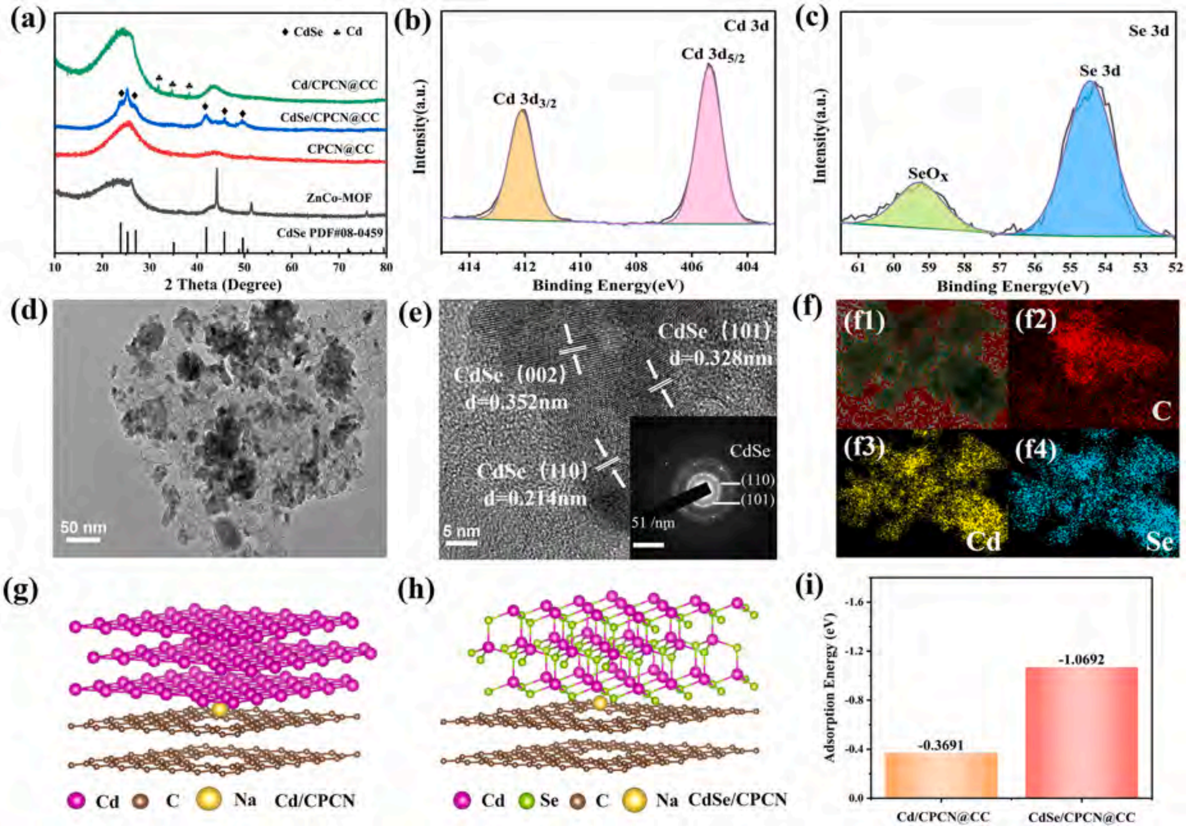

Fig. 4. (a) XRD spectra of ZnCo-MOF, CPCN@CC, Cd/CPCN@CC, and CdSe/CPCN@CC; XPS spectra of (b) Cd 3d of CdSe, (c) Se 3d of CdSe and (d) TEM image and HR-TEM image and SAED pattern of CdSe/CPCN composite; (f) (f1)total EDS element mapping and the corresponding EDS mappings of C (f2), Cd (f3), Se (f4) elements of CdSe/CPCN composite; Sodium ion adsorption model of (g) Cd/CPCN composite and (h) CdSe/CPCN composite; (i) absorption energy of Cd/CPCN@CC and CdSe/CPCN@CC.

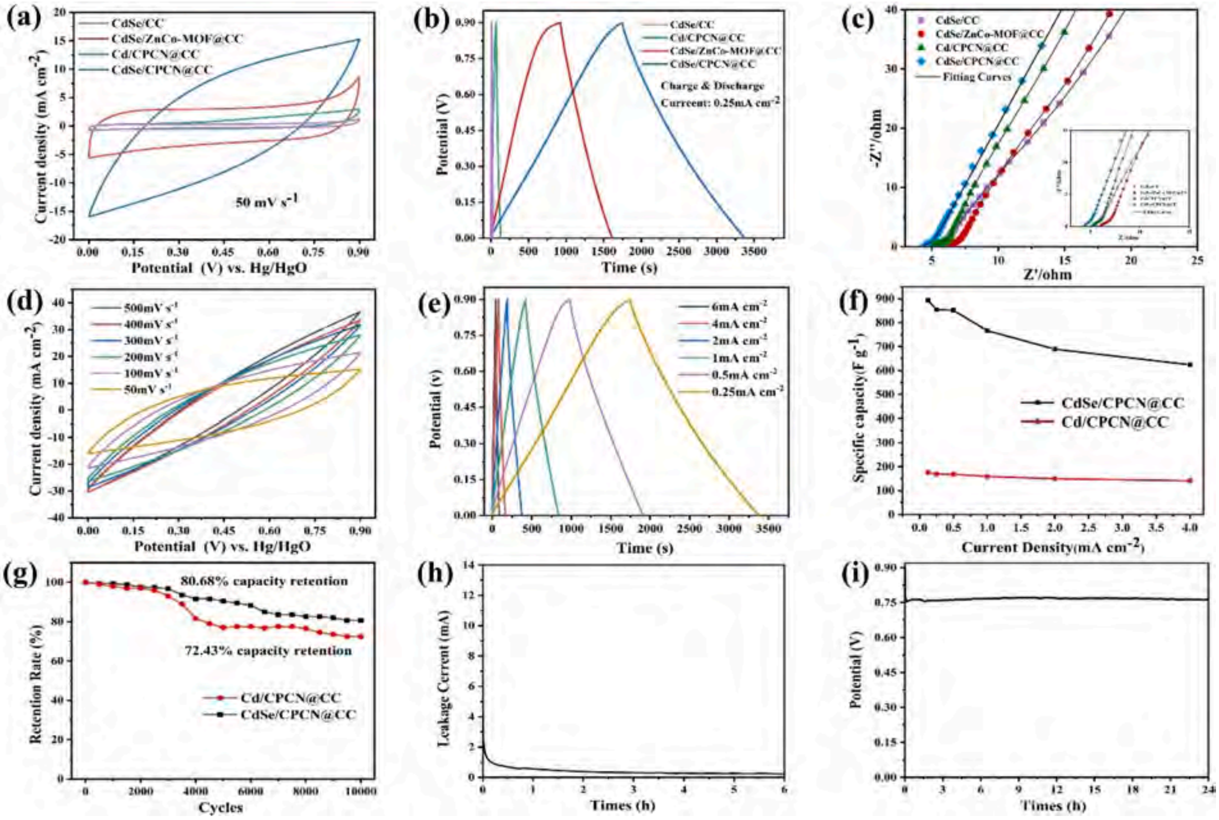

Fig. 5. (a) CV curves (b) GCD curves and (c) Nyquist plots curves of CdSe/CC, CdSe/ZnCo-MOF@CC, Cd/CPCN@CC and CdSe/CPCN@CC; (d) CV curves and (e) GCD curves of CdSe/CPCN@CC; (f) Specific capacity at different current densities and (g) Long-term performance under a GCD current density of 6 mA cm^{-2} of Cd/CPCN@CC and CdSe/CPCN@CC; (h) leakage current and (i) self-discharge performance of CdSe/CPCN@CC.

ZnCo/Carbon@CC. Zn and Co in the carbonized MOF dissolve during acid etching to form the conductive porous carbon nanosheets. The CdSe/CPCN@CC composite is synthesized by a hydrothermal method with CPCN@CC as the substrate and $CdCl_2 \cdot 6H_2O$ and selenium powder as the actants.

CV, GCD, and EIS are performed using a three-electrode system in 1.0 M Na_2SO_4 as the electrolyte. Fig. 2(a)–(c) show that CPCN@CC has a longer discharging time, larger CV area, smaller contact resistance, and higher ion diffusion efficiency than CC and ZnCo-MOF@CC. The stability of CPCN@CC and ZnCo-MOF are presented in Fig. 2(d). The retention rate of ZnCo-MOF@CC is 71.43% after 10,000 charging and discharging cycles, while CPCN@CC shows higher retention of 86.72% due to the robust carbon structure and efficient ion diffusion. Fig. 2(e) shows the CV curves of CPCN@CC between 50 mV s^{-1} and 500 mV s^{-1} revealing a rectangular shape with an increasing trend as the scanning rate increases, showing good reaction kinetics [47,48]. Fig. 2(f) displays the GCD results of CPCN@CC from 0.25 mA cm^{-2} to 6 mA cm^{-2}. The curve have an isosceles triangular shape with good symmetry indicative of high Coulombic efficiency and good reversibility.

Fig. 3(a) and (b) depict the SEM images of ZnCo-MOF at different magnifications. The ZnCo-MOF sheets are grown evenly and orderly on the carbon cloth, and the 3D structure has a thickness of 120~170 nm and length of 1.5 μm. Fig. 3(c) and (d) show that the thickness of ZnCo-MOF is about 50 nm after annealing in N_2. The reduced MOF sheet thickness caused by precursor decomposition during calcination results in lower electrical resistance due to the shorter transport distance for electrons and ions. Moreover, annealing enhances both the stability and adhesion of the MOF precursor to CC, since the precursor structure remains stable after the hydrothermal reaction. Fig. 3(e) and (f) show that etching produces porous structure on the carbon surface derived from MOFs, thereby increasing the surface area of the CPCN@CC nanocomposite. Fig. 3(g) and (h) reveal a uniform distribution of CdSe nanoparticles on the MOF sheets with an average particle diameter of 180-260 nm. The nanoscale CdSe particles in combination with CPCN improve the contact area and conductivity, and the loading capacity of CdSe per unit area increases. In comparison, Fig. 3(i) and (j) show that on Cd/CC, Cd nanorods about 200-500 nm in length are clustered on the surface of the carbon cloth. Fig. 3(k) and (l) confirm the smaller loading of Cd without the nanoscale structure.

Fig. 4(a) presents the XRD patterns of ZnCo-MOF, CPCN@CC, Cd/CPCN@CC, and CdSe/CPCN@CC. The diffraction peaks of Co and Zn from ZnCo-MOF (black) are in good agreement with previous reports [31,49,50], corroborating synthesis of ZnCo-MOF. The Co and Zn peaks are not observed from CPCN@CC (red) due to the removal of Co and Zn from the ZnCo-MOF precursor. Cd/CPCN@CC (green) shows peaks at 31.83°, 34.74°, and 38.35° corresponding to the (002), (100), and (101) planes of Cd (PDF#05–0674). CdSe/CPCN@CC (blue) shows peaks CdSe at 23.90°, 25.35°, 41.97°, 45.79°, and 49.67° associated with the (100), (002), (110), (103), and (112) planes of CdSe (PDF#08–0459). As shown in Fig. 4(b), the two peaks in the Cd 3*d* spectrum at 412.8 eV and 405.27 eV confirm the presence of Cd [12,50,51]. The peak at 54-55 eV in Fig. 4(c) belongs to Se 3*d*, and that at 58-60 eV is related to SeO_x from surface oxidation [12,52]. As shown in Fig. S2, EDS shows the presence of Cd, Se, and C.

Fig. 4(d) shows the morphology of the CPCN carbon nanosheets and CdSe nanoparticles, and the nanoparticle sizes are consistent with those observed by SEM. Fig. 4(e) reveals the (002), (101), and (110) planes with d-spacings of 3.52 Å, 3.28 Å, and 2.14 Å, respectively. The selected-area electron diffraction (SAED) pattern (Fig. 4(h)) of CdSe/CPCN@CC shows concentric rings indicative of the polycrystalline nature with the corresponding (101) and (110) planes at the ring diameter. The elemental maps in (f2)–(f4) of Fig. 4(f) indicate uniform distributions of cadmium, selenium, and carbon. Fig. S3 displays that the weight percentages of the carbon in CdSe/CPCN@CC was estimated to be 91.7%,

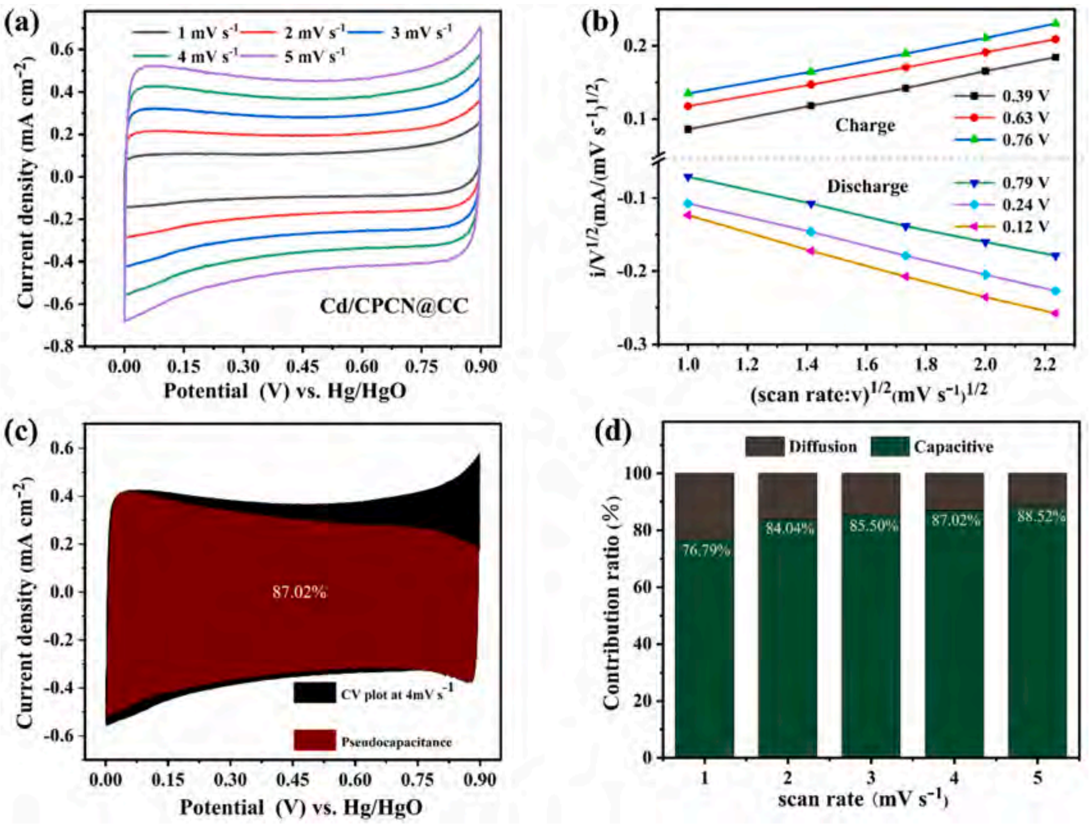

Fig. 6. (a) CV curves of Cd/CPCN@CC; (b) 6 selected sets of CV data obtained at different voltages for the calculation of k_1 by Eq. (5); (c) Pseudocapacitance of the Cd/CPCN@CC at 4 mV s^{-1}; (d) Pseudocapacitance contribution ratios.

based on the chemical reaction between CdSe and O_2 with the generation of CdO and SeO_2. This is consistent with the data obtained by EDS data (C: 91.4%, Se:4.4%, Cd:4.2%). Fig. 4(g) and (h) present the adsorption models of Cd and CdSe for sodium ions on the conductive porous carbon structure. The calculated sodium adsorption energies (E_{ad}) of Cd/CPCN and CdSe/CPCN are -0.3691 eV and -1.0692 eV, respectively (Fig. 4(i)). Compared with the composite structure of Cd, CdSe has a lower E_{ad}, higher adsorption capacity, and faster Na ion storage kinetics.

Fig. 5(a) and (b) show that the electrochemical properties of CdSe/CC, CdSe/ZnCo-MOF@CC, Cd/CPCN@CC, and CdSe/CPCN@CC are comparable. However, CdSe/CPCN@CC displays a larger CV area and longer discharging time than CdSe/CC, CdSe/ZnCo-MOF@CC, and Cd/CPCN@CC. The discharging time of CdSe/CPCN@CC at a current density of 0.25 mA cm^{-2} is 1,595 s, but CdSe/CC, CdSe/ZnCo-MOF@CC and Cd/CPCN@CC show discharging times of only 12 s, 61s, and 684.4 s, respectively. Based on the mass difference before and after deposition, the CdSe loading of the CdSe/CPCN@CC composite is calculated to be 2.4 mg cm^{-2}. According to Fig. 5(b) and Eq. (2), the specific capacity of CdSe/CPCN@CC is 854.63 F g^{-1} at a current density of 0.25 mA cm^{-2}, which is approximately five times greater than that of Cd/CPCN@CC (168.89 F g^{-1}). The porous frame and materials play important roles in the performance of supercapacitors. Fig. 5(c) reveals that CdSe/CPCN@CC has the smallest radius in the high-frequency region and smaller charge transfer resistance. Furthermore, CdSe/CPCN@CC shows the largest slope in the low-frequency region, suggesting excellent diffusion ability.

The electron transfer process of CdSe during charging and discharging is described as follows [53]:

$CdSe + 2Na^{+} + 2e^{-} \rightarrow Cd + Na_2Se$ and

$Cd + 3Na^{+} + 3e^{-} \rightarrow Na_3Cd$.

The specific capacitance (Cs) can be calculated by Eq. (2), and the energy (E) and power (P) density can be determined by Eqs. (3) and (4) [54]:

$$Cs = \frac{I \times \Delta t}{m \times \Delta V} \tag{2}$$

$$E = \frac{C \times (\Delta V)^2}{2 \ast 3.6} \tag{3}$$

$$P = \frac{E \ast 3600}{\Delta t}, \tag{4}$$

where C_s (F g^{-1}) is the specific capacitance, I (A) is the current density during charging and discharging, Δt (s) is the discharging time, m (g) is the mass of the active substance in the electrode, and ΔV (V) is the pressure drop in the test. As shown in Fig. 5(d), the CV curves of CdSe/CPCN@CC has a rectangular shape and increase gradually as the scanning rates go up from 50 mV s^{-1} to 500 mV s^{-1}. The CV curves all show a similar shape, indicating that the CdSe/CPCN@CC electrodes remain stable during the cycles [55]. Fig. S4 shows that at the same scanning rate, the area under the CV curve of CdSe/CPCN@CC is larger than that of Cd/CPCN@CC, indicating a stronger charge storage capacity [56]. Fig. 5(e) shows the GCD curve of CdSe/CPCN@CC from 0.25 mA cm^{-2} to 6.0 mA cm^{-2}. It exhibits a similar isosceles triangular shape with good symmetry. The voltage and current of CdSe/CPCN@CC are linear during discharging, suggesting good reversibility and high Coulombic efficiency. Fig. S5 shows that the discharging time of CdSe/CPCN@CC is longer than that of Cd/CPCN@CC at the same current density consistent with CV. Fig. 5(f) illustrates the relationship between the specific capacity and current density of both Cd/CPCN@CC and CdSe/CPCN@CC. The specific capacitances of CdSe/CPCN@CC are 893.52 F g^{-1}, 854.63 F g^{-1}, 851.85 F g^{-1}, 766.67 F g^{-1}, 689.26 F g^{-1}, and 623.71 F g^{-1} at current

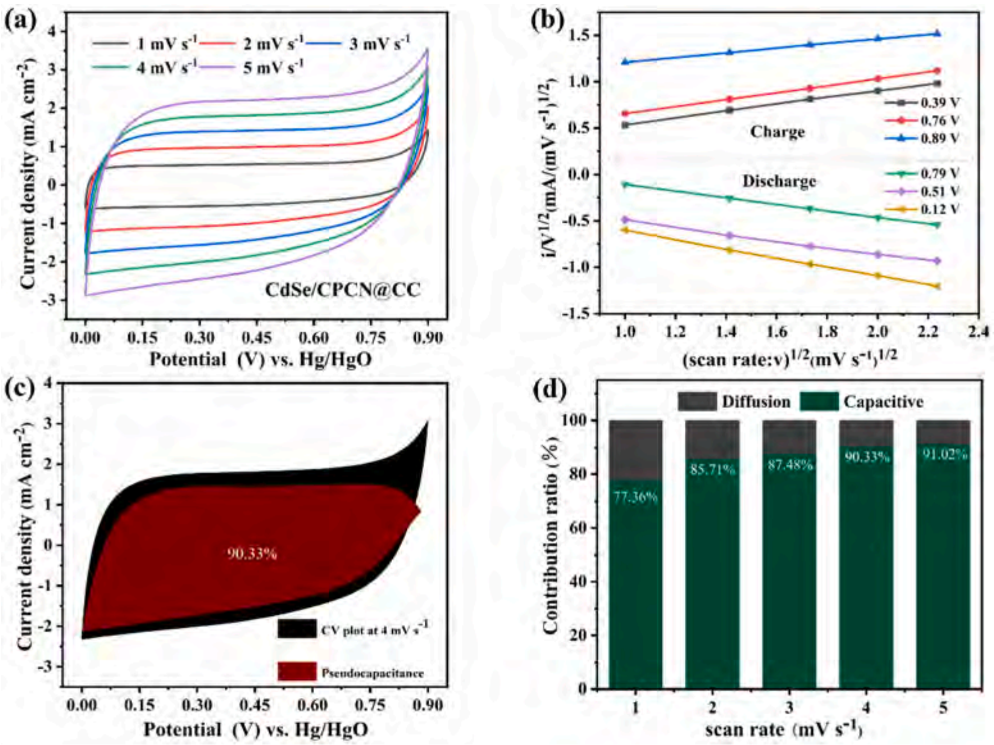

Fig. 7. (a) CV curves of CdSe/CPCN@CC; (b) 6 selected sets of CV data obtained at different voltages for the calculation of k_1 by Eq. (5); (c) Pseudocapacitance of the CdSe/CPCN@CC at 4 mV s^{-1}; (d) Pseudocapacitance contribution ratios.

densities of 0.125 mA cm^{-2}, 0.25 mA cm^{-2}, 0.5 mA cm^{-2}, 1 mA cm^{-2}, 2 mA cm^{-2}, and 4 mA cm^{-2}, respectively. In comparison, Cd/CPCN@CC shows capacitances of 176 F g^{-1}, 168.89 F g^{-1}, 168.62 F g^{-1}, 159.11 F g^{-1}, 149.69 F g^{-1}, and 141.51 F g^{-1} at current densities of 0.125 mA cm^{-2}, 0.25 mA cm^{-2}, 0.5 mA cm^{-2}, 1 mA cm^{-2}, 2 mA cm^{-2}, and 4 mA cm^{-2}, respectively.

Fig. 5(g) illustrates the stability of Cd/CPCN@CC and CdSe/CPCN@CC for 10,000 GCD cycles showing capacitance retention of 80.68% for CdSe/CPCN@CC, which is better than 72.43% of Cd/CPCN@CC. The leakage current and self-discharging are important factors for electrodes. The CdSe/CPCN@CC electrode is first charged to 0.9 V and maintained at this voltage for 6 h to measure the leakage current, as shown in Fig. 5(h). The leakage current decreases rapidly from 12.74 mA to 0.87 mA within 0.25 h but stabilizes at 0.18 mA due to a smaller amount of impurities and few shuttle reactions [57]. To monitor the self-discharging of CdSe/CPCN@CC, measurements are made under open circuit conditions for 24 h [4,58]. Owing to the leakage current, the potential decreases gradually with time, and it is an especially significant drop in the first 2 h. As shown in Fig. 5(i), the potential-time curves indicate a stable output potential of 0.76 V after 2 h and a good self-discharge rate remaining at around 0.76 V after 24 h.

To explore the mechanism of Cd/CPCN@CC and CdSe/CPCN@CC, the pseudocapacitances are calculated from the CV plots in Figs. 6(a) and 7(a) and by calculating k_1 (Figs. 6(b) and 7(b)) [59] by Eq. (5):

$$\frac{i(V)}{v^{\frac{1}{2}}} = k_1 v^{\frac{1}{2}} + k_2, \tag{5}$$

where i(V) is the CV current at the selected voltage (V), v is the scanning rate, k_1 is equal to the slope of each curve in Figs. 6(a) and 7(a), and the current for the pseudocapacitance at different voltages is determined by k_1v. Taking k_1v as the ordinate and the corresponding voltage as the abscissa, the pseudocapacitance (red area) is shown in Figs. 6(c) and 7(c) and the relative pseudo-capacitance contributions at different scanning rates are summarized in Figs. 6(d) and 7(d). The pseudocapacitance ratio of Cd/CPCN@CC calculated from the CV data is 76.79% when the scanning rate is 1 mV s^{-1}, and 88.52% when the scanning rate is 5 mV s^{-1}. The pseudocapacitance of CdSe/CPCN@CC can be derived from Fig. 7(c). The proportion of pseudocapacitance contribution of CdSe/CPCN@CC at each scanning rate between 1 mV s^{-1} and 5 mV s^{-1} is summarized in Fig. 7(d). CdSe/CPCN@CC shows larger pseudocapacitance contributions than Cd/CPCN@CC. For example, at a

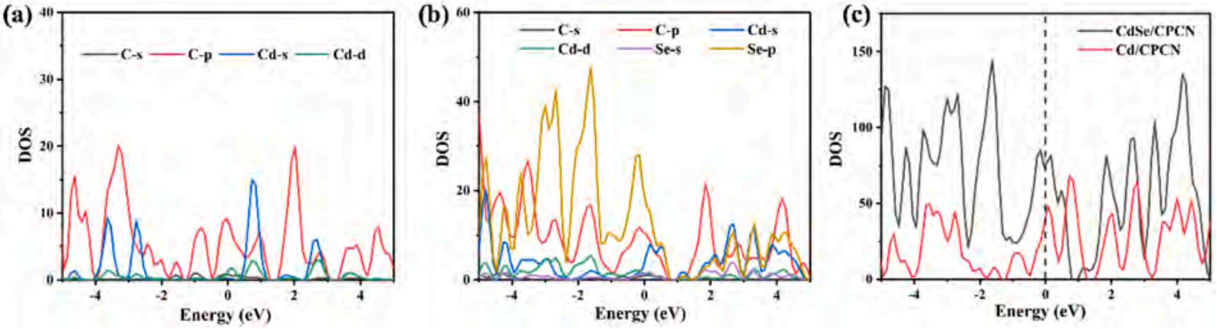

Fig. 8. (a) PDOS of Cd/CPCN@CC; (b) PDOS of CdSe/CPCN@CC ; (c) TDOS of Cd/CPCN@CC and CdSe/CPCN@CC.

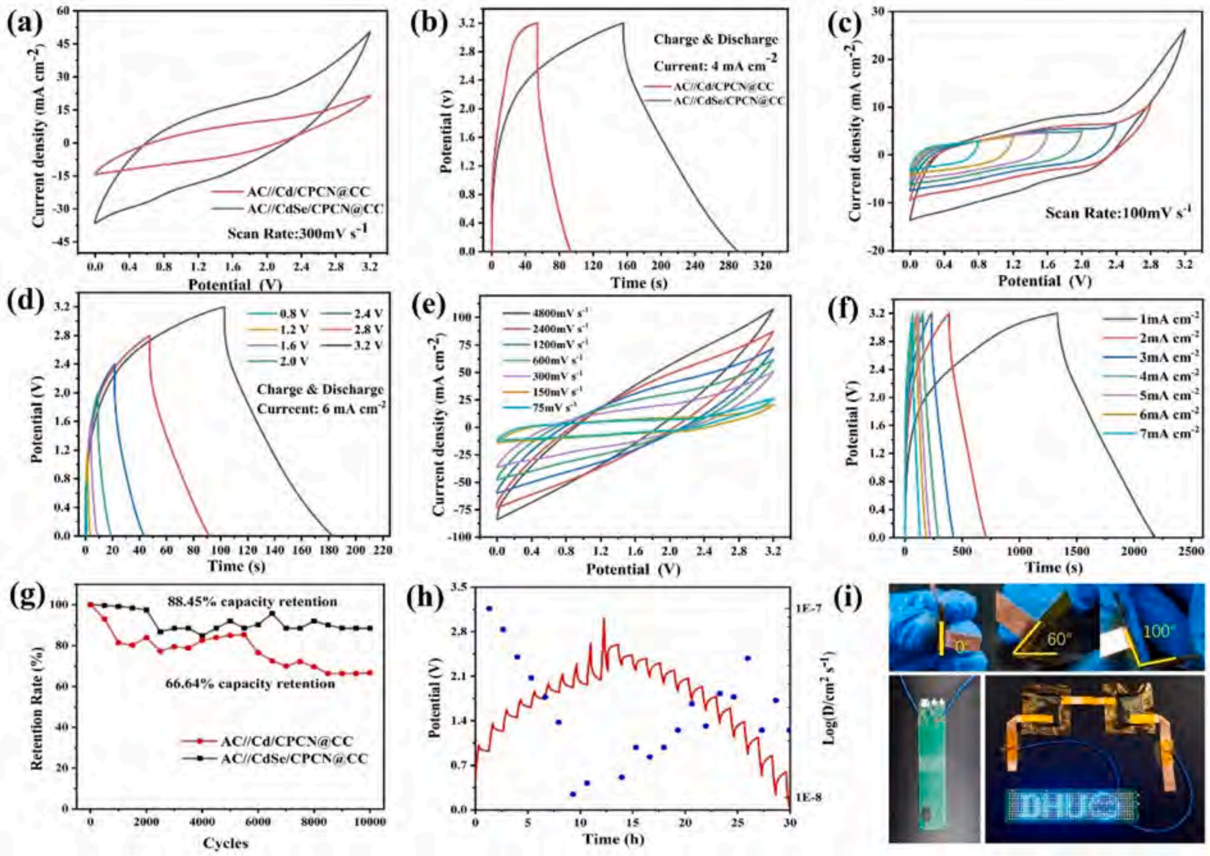

Fig. 9. (a) CV curves at 300 mV s^{-1} and (b) GCD curves at 4 mA cm^{-2} of AC//CdSe/CPCN@CC and AC//Cd/CPCN@CC; (c) CVcurves and (d) GCD curves with different upper cut-off voltages, (e) CV curves acquired at different scanning rates and (f) GCD curves for different current densities of AC//CdSe/CPCN@CC; (g) Long-term performance of AC//CdSe/CPCN@CC and AC//Cd/CPCN@CC; (h) GITT curve and the corresponding Na$^+$ diffusion coefficient of AC//CdSe/CPCN@CC; (i) A flexible supercapacitor device is bended at different angles and two of these devices are connected in parallel to provide power supply for programmable LED arrays.

scanning rate of 4 mV s^{-1}, the pseudocapacitance contribution of CdSe/CPCN@CC is 90.33% which is higher than that of Cd/CPCN@CC (87.02%). Hence, the CdSe/CPCN@CC electrode has better pseudocapacitance characteristics.

We further investigated the projected density of states (PDOS) and total density of states (TDOS) of Cd/CPCN@CC and CdSe/CPCN@CC and the results are presented in Fig. 8(a)–(c). Fig. 8(a) illustrates that both the C 2*p* and Cd 4*d* orbitals intersect the Fermi level. Additionally, there is a peak in the Cd 5*s* orbital at 0.72 eV, while the C 2p orbital shows peaks at -0.8 eV and 2.03 eV. Therefore, the states near the Fermi level are influenced by the C 2*p* and Cd 5*s* states. Fig. 8(b) shows the Se 4*p* and Cd 5*s* orbitals cross the Fermi level. There are a Se 4*p* peak at -1.62 eV, a splitting peak of Cd 5*s* at 0.16 eV, and a C 2*p* peak at 1.85 eV. The states near the Fermi level are mainly Se 4*p*, C 2*p*, and Cd 5*s*. Fig. 8 (c) exhibits the TDOS of the two materials. Compared with previous reports [60], when CdSe is combined with porous carbon, the bandgap decreases, the Fermi level moves down, and the hole concentration increases, thereby improving the conductivity. Moreover, the number of electrons near the Fermi level is larger, consequently facilitating electron transport and enabling fast reaction kinetics. These results explain why CdSe/CPCN@CC delivers enhanced electrochemical performance.

The hybrid asymmetric supercapacitor is assembled in the 1 M $NaPF_6$ electrolyte with either CdSe/CPCN@CC (AC//CdSe/CPCN@CC) or Cd/CPCN@CC (AC//Cd/CPCN@CC) as the positive electrode and the active carbon-based nickel foam as the negative electrode. Fig. 9(a) and (b) show the electrochemical characteristics of the asymmetric supercapacitor. The CV area of AC//CdSe/CPCN@CC is larger than that of AC//Cd/CPCN@CC for the same current density. At the current density is 4 mA cm^{-2}, the discharging time of AC//CdSe/CPCN@CC is almost 3.5 times longer than that of AC//Cd/CPCN@CC. The CV and GCD curves of AC//CdSe/CPCN@CC obtained in different potential windows are presented in Fig. 9(c) and (d). In the voltage window of 0-3.2V, there are no obvious changes in the curves, indicating that the positive and negative electrodes match well to broaden the working potential. For comparison, the GCD and CV curves of AC//Cd/CPCN@CC in different potential windows are exhibited in Figs. S6 and S7. As shown in Fig. 9(e), the CV curves of AC//CdSe/CPCN@CC obtained at different scanning rates from 75 mV s^{-1} to 4,800 mV s^{-1} show that the device can withstand a high scanning rate of 4,800 mV s^{-1} without distortion. All curves have the same shape, and the current density increases with the increase of scanning speed, indicating that the CdSe/CPCN@CC complex has excellent speed and stability [61,62].

The GCD curves acquired at different current densities (Fig. 9(f)) show a triangular shape, so the device has good electrochemical characteristics, fast I–V response, and excellent electrochemical reversibility.

The CV and GCD data of AC//Cd/CPCN@CC are presented in Figs. S8 and 9. AC//CdSe/CPCN@CC shows a longer discharging time and larger CV area than AC//Cd/CPCN@CC. Based on Eqs. (2)–(4), at a current density of 4 mA cm^{-2}, AC//Cd/CPCN@CC has a capacitance of 17.25 F g^{-1}, energy density of 24.53 Wh kg^{-1}, and power density of 2264.31W kg^{-1}. On the other hand, AC//CdSe/CPCN@CC composite shows a capacitance of 62.3 F g^{-1}, an energy density of 88.61 Wh kg^{-1}, and a power density of 2,359.44 W kg^{-1} under the same conditions. The capacitance of AC//CdSe/CPCN@CC is 97.8 F g^{-1}, energy density is 139.10Wh kg^{-1}, and power density is 589.82W kg^{-1} at 1 mA cm^{-2}. The specific capacity, energy densities and power densities of AC//CdSe/CPCN@CC under

Table 1
Comparison of the as-assembled supercapacitors with those reported in the literature.

Electrodes	Potential Window (V)	Specific Capacitance (F g^{-1})	Energy Density (Wh kg^{-1})	Power Density (W kg^{-1})	Capacitive Retention	Refs.
3DG/$CoSe_2$-$SnSe_2$//AC	1.5	38	11.89	749.9	91.9%@3000cycles	[63]
$Co_{0.85}Se$ -16h//AC	1.8V	—	44.2	888.9	91.9%@6500cycles	[64]
CoSe//AC	1.5V	—	17.6	684	95.5%@2000cycles	[65]
CdSe@PbS//CdSe@PbS	1V	—	16.14	288	79%@5000 cycles	[66]
CdSe/CPCN@CC//AC	4V	62.3	88.61	2359.44	88.45%@10000 cycles	this work
Cd/CPCN@CC//AC	4V	17.25	24.53	2264.31	66.64%@10000 cycles	this work

different current densities are shown in Table S1. A higher energy density is achieved in comparison with previous results (Table 1), for example, 3DG/$CoSe_2$-$SnSe_2$//AC (specific capacitance 38 F g^{-1} and 11.89 Wh kg^{-1} at a power density of 749.9 W kg^{-1}) [63], $Co_{0.85}Se$ -16h//AC (41.8 Wh kg^{-1} at 750 W kg^{-1}) [64], CoSe//AC (17.6 Wh kg^{-1} at 684 W kg^{-1}) [65], and CdSe@PbS//CdSe@PbS (16.14 Wh kg^{-1} at 288 W kg^{-1}) [66].

According to the EIS results in Fig. S10, AC//CdSe/CPCN@CC has the smallest arc radius and largest slope in the low-frequency region, implying lower impedance and higher ion mobility in agreement with the results obtained by CV and GCD. Fig. 9(g) shows the cycling stability of the supercapacitor. After 10,000 cycles, the AC//CdSe/CPCN@CC supercapacitor retains 88.45% of its initial specific capacitance, whereas the AC//Cd/CPCN@CC supercapacitor retains only 66.64% of the initial capacitance. The diffusion coefficient of Na^+ was measured by the GITT and calculated according to the simplified formula [67]

$$D = \frac{4L^2}{\pi\tau}\left(\frac{\Delta E_s}{\Delta E_t}\right)^2 \tag{6}$$

where τ is the relaxation time (s), ΔE_S is the change of potential (V) caused by the current pulse, and ΔE_t is the change of potential (V) during constant current discharge without iR drop. L is the sodium ion diffusion path length (cm), which can be simply expressed as the electrode thickness. The GITT profile and corresponding Na^+ diffusion coefficient are shown in Fig. 9(h), the D_{Na+} values mainly concentrate in 10^{-8} cm^2 s^{-1}, which is considered to be relatively high for Na^+ diffusion, further explaining the rapid reaction kinetics and excellent energy storage performance of the composites. Fig. 9(i) demonstrates that the replacement of foam nickel with carbon cloth as the negative electrode in the device improves the flexibility. The supercapacitor can withstand large mechanical deformation such as large bending angles. An LED array (11*44) can be powered by two flexible devices in series after charging at a large current for a few seconds. The device thus has large potential in flexible and wearable applications.

4. Conclusion

Nanoscale CdSe nanoparticles are fabricated on conductive porous carbon nanoflakes (CPCN) derived from ZnCo-MOFs to form flexible electrodes for high-performance sodium-ion supercapacitors. The CdSe nanoparticles in the 3D CPCN structure prevent fragmentation and aggregation of the nanoparticles while enhancing electron transfer and Na^+ diffusion. DFT calculations reveal that the CdSe/CPCN composite enhances the adsorption of sodium ions as well as the conductivity of the electrode. The CdSe/CPCN composite is fabricated on carbon cloth to form a flexible electrode for supercapacitors. Electrochemical assessment utilizing a three-electrode system reveals remarkable pseudocapacitive features, fast I-V response, and excellent reversibility. The hybrid device is highly durable, being able to withstand a high scanning rate of 4800 mV s^{-1}. Moreover, it shows energy densities of 139.10 Wh kg^{-1} and 72.36 Wh kg^{-1} at power densities of 589.82 W kg^{-1} and 4,128.31 W kg^{-1}, respectively. The flexible supercapacitor can withstand large mechanical deformation such as large bending angles, and an LED array can be powered by two flexible devices in series after charging at a large current for a few seconds. The results suggest that the CdSe/CPCN@CC electrode has large potential in energy storage applications.

CRediT authorship contribution statement

Hanxue Zhao: Conceptualization, Formal analysis, Data curation, Methodology, Validation, Visualization, Writing – original draft. **Mai Li:** Conceptualization, Formal analysis, Methodology, Funding acquisition, Project administration, Resources, Supervision, Validation, Visualization, Writing – review & editing. **Jintao Du:** Software. **Yuhang Lei:** Software. **Ayesha Irfan:** Investigation. **Muhammad Imran:** Investigation. **Chunrui Wang:** Resources. **Jun He:** Investigation. **Zhongyi Sun:** Investigation. **Paul K. Chu:** Funding acquisition, Writing – review & editing.

Declaration of Competing Interest

The authors declare the following financial interests/personal relationships which may be considered as potential competing interests:

Mai Li reports financial support was provided by Donghua University. Paul K. Chu reports financial support was provided by City University of Hong Kong. If there are other authors, they declare that they have no known competing financial interests or personal relationships that could have appeared to influence the work reported in this paper.

Data availability

Data will be made available on request.

Acknowledgments

The research was funded by the National Natural Science Foundation of China (grant number 22005046), City University of Hong Kong Donation Research Grants (DON-RMG 9229021 and 9220061), and City University of Hong Kong Strategic Research Grant (SRG) (No. 7005105).

Supplementary materials

Supplementary material associated with this article can be found, in the online version, at doi:10.1016/j.electacta.2023.143366.

References

[1] I. Hussain, C. Lamiel, M.S. Javed, M. Ahmad, S. Sahoo, X. Chen, N. Qin, S. Iqbal, S. Gu, Y. Li, C. Chatzichristodoulou, K. Zhang, MXene-based heterostructures: current trend and development in electrochemical energy storage devices, Prog. Energy Combust. Sci. 97 (2023), 101097.

[2] I. Hussain, M.Z. Ansari, C. Lamiel, T. Hussain, M.S. Javed, T. Kaewmaraya, M. Ahmad, N. Qin, K. Zhang, *In situ* grown heterostructure based on MOF-derived

carbon containing n-type Zn–In–S and dry-oxidative p-type CuO as pseudocapacitive electrode materials, ACS Energy Lett. 8 (2023) 1887–1895.

[3] I. Hussain, C. Lamiel, M. Sufyan Javed, M. Ahmad, X. Chen, S. Sahoo, X. Ma, M. A. Bajaber, M. Zahid Ansari, K. Zhang, Earth- and marine-life-resembling nanostructures for electrochemical energy storage, Chem. Eng. J. 454 (2023), 140313.

[4] M. Li, K.L. Zhu, H.X. Zhao, Z.Y. Meng, C.R. Wang, P.K. Chu, Construction of alpha-MnO_2 on carbon fibers modified with carbon nanotubes for ultrafast flexible supercapacitors in ionic liquid electrolytes with wide voltage windows, Nanomaterials 12 (2022) 2020.

[5] I. Hussain, S. Iqbal, T. Hussain, Y. Chen, M. Ahmad, M.S. Javed, A. AlFantazi, K. Zhang, An oriented Ni–Co-MOF anchored on solution-free 1D CuO: a p–n heterojunction for supercapacitive energy storage, J. Mater. Chem. A 9 (2021) 17790–17800.

[6] V. Nisha, A. Paravannoor, D. Panoth, S.T. Manikkoth, K.M. Thulasi, S. Palantavida, B.K. Vijayan, CdS nanosheets as electrode materials for all pseudocapacitive asymmetric supercapacitors, Bull. Mater. Sci. 44 (2021) 101.

[7] Z.Z. Zhai, L.H. Zhang, T.M. Du, B. Ren, Y.L. Xu, S.S. Wang, J.F. Miao, Z.F. Liu, A review of carbon materials for supercapacitors, Mater. Des. 221 (2022), 111017.

[8] D. Zhang, C. Tan, W.Z. Zhang, W.J. Pan, Q. Wang, L. Li, Expanded graphite-based materials for supercapacitors: a review, Molecules 27 (2022) 716.

[9] G.P. Ojha, G.W. Kang, Y.S. Kuk, Y.E. Hwang, O.H. Kwon, B. Pant, J. Acharya, Y. W. Park, M. Park, Silicon carbide nanostructures as potential carbide material for electrochemical supercapacitors: a review, Nanomaterials 13 (2023) 150.

[10] A.F. Liu, L. Tang, L. Gong, S.J. Wu, J.X. Tang, Decorating cobalt selenide nanoparticles on polypyrrole nanowires as nanocomposite electrodes for hybrid supercapacitors, J. Electroanal. Chem. 923 (2022), 116734.

[11] A. Amiri, A. Bruno, A.A. Polycarpou, Configuration-dependent stretchable all-solid-state supercapacitors and hybrid supercapacitors, Carbon Energy 5 (2023) e320.

[12] L.X. Teng, L.C. Tian, W.F. Li, H.M. Feng, Z.C. Xing, Preparation and characterization of CdSe as electrode materials for supercapacitors, Synth. Met. 291 (2022), 117169.

[13] X. Li, X.H. Sun, X.D. Hu, F.R. Fan, S. Cai, C.M. Zheng, G.D. Stucky, Review on comprehending and enhancing the initial Coulombic efficiency of anode materials in lithium-ion/sodium-ion batteries, Nano Energy 77 (2020), 105143.

[14] Y.A. Kumar, G. Koyyada, T. Ramachandran, J.H. Kim, S. Sajid, M. Moniruzzaman, S. Alzahmi, I.M. Obaidat, Carbon materials as a conductive skeleton for supercapacitor electrode applications: a review, Nanomaterials 13 (2023) 1049.

[15] W. Wang, J. Cao, J.W. Yu, F.J. Tian, X.Y. Luo, Y.T. Hao, J.Y. Huang, F.C. Wang, W. Q. Zhou, J.K. Xu, X.M. Liu, H.J. Yang, Flexible supercapacitors based on stretchable conducting polymer electrodes, Polymers 15 (2023) 1856.

[16] W.L. Luo, Y. Ma, T.X. Li, H.K. Thabet, C.P. Hou, M.M. Ibrahim, S.M. El-Bahy, B. B. Xu, Z.H. Guo, Overview of MXene/conducting polymer composites for supercapacitors, J. Energy Storage 52 (2022), 105008.

[17] A. Pramitha, Y. Raviprakash, Recent developments and viable approaches for high-performance supercapacitors using transition metal-based electrode materials, J. Energy Storage 49 (2022), 104120.

[18] X. Zhao, W. Cai, Y. Yang, X.D. Song, Z. Neale, H.E. Wang, J.H. Sui, G.Z. Cao, $MoSe_2$ nanosheets perpendicularly grown on graphene with Mo-C bonding for sodium-ion capacitors, Nano Energy 47 (2018) 224–234.

[19] J. Liu, J. Xie, H.L. Dong, H.X. Wei, C.C. Sun, J. Yang, H.B. Geng, Iron doping of $NiSe_2$ nanosheets to accelerate reaction kinetics in sodium-ion half/full batteries, Sci. China Mater. 66 (2023) 69–78.

[20] H.J. Zhou, X.X. Li, Y. Li, M.B. Zheng, H. Pang, Applications of M_xSe_y (M=Fe, Co, Ni) and their composites in electrochemical energy storage and conversion, Nanomicro Lett. 11 (2019) 40.

[21] X.R. Yun, T. Lu, R.Y. Zhou, Z.H. Lu, J.Y. Li, Y.R. Zhu, Heterostructured $NiSe_2$/$CoSe_2$ hollow microspheres as battery-type cathode for hybrid supercapacitors: electrochemical kinetics and energy storage mechanism, Chem. Eng. J. 426 (2021), 131328.

[22] Y.R. Zhu, H. Tang, X.R. Yun, L.J. Xi, Z.L. Hu, One-pot hydrothermal synthesis of 3D Cu_2Se/CoSe composite as a novel battery-type cathode material with enhanced capacitive properties, J. Alloys Compd. 866 (2021), 158972.

[23] T. Lu, S.M. Dong, C.J. Zhang, L.X. Zhang, G.L. Cui, Fabrication of transition metal selenides and their applications in energy storage, Coord. Chem. Rev. 332 (2017) 75–99.

[24] M. Safdar, M. Awais, S. Muneer, S. Gouadria, N. Jabeen, M. Iftikhar, M. Waqas, S. Aslam, Javaria, M. Asghar, M. Mirza, M.B. Tahir, Solvothermal synthesis of Al_2Se_3/rGO nanocomposites with excellent electrochemical performance in supercapacitor, J. Energy Storage 65 (2023), 107160.

[25] S.M. Bekhit, S.G. Mohamed, I.M. Ghayad, S.Y. Attia, W. Metwally, R. Abdel-Karim, S.M. El-Raghy, Snow crystal-like structure of NiSe as a binder-free electrode for high-performance hybrid supercapacitor, J. Mater. Sci. 57 (2022) 9955–9970.

[26] C.Y. Hui, C.W. Kan, C.L. Mak, K.H. Chau, Flexible energy storage system-an introductory review of textile-based flexible supercapacitors, Processes 7 (2019) 922.

[27] X.H. Wang, B. Shi, Y. Fang, F. Rong, F.F. Huang, R.H. Que, M.W. Shao, High capacitance and rate capability of a Ni_3S_2@CdS core-shell nanostructure supercapacitor, J. Mater. Chem. A 5 (2017) 7165–7172.

[28] S.L. Patil, S.S. Raut, B.R. Sankapal, $Cu(OH)_2$@$Cd(OH)_2$ core-shell nanostructure: synthesis to supercapacitor application, Thin Solid Films 692 (2019), 137584.

[29] A.U. Khan, K. Tahir, M.Z.U. Shah, M.Y. Khalil, Z.M. Almarhoon, H.M.A. Hassan, F. Abdulaziz, A.A. Alanazi, A.A. El-Zahhar, A.M. Munshi, A new cadmium oxide (CdO) and copper selenide (CuSe) nanocomposite: an energy-efficient electrode for wide-voltage hybrid supercapacitors, Colloids Surf. A Physicochem. Eng. Asp. 656 (2023), 130327.

[30] I. Rathinamala, I.M. Babu, J.J. William, G. Muralidharan, N. Prithivikumaran, CdS microspheres as promising electrode materials for high performance supercapacitors, Mater. Sci. Semicond. Process. 105 (2020), 104677.

[31] D. He, Y. Gao, Y.C. Yao, L. Wu, J. Zhang, Z.H. Huang, M.X. Wang, Asymmetric supercapacitors based on hierarchically nanoporous carbon and $ZnCo_2O_4$From a single biometallic metal-organic frameworks (Zn/Co-MOF), Front. Chem. 8 (2020) 719.

[32] N.L. Torad, R.R. Salunkhe, Y.Q. Li, H. Hamoudi, M. Imura, Y. Sakka, C.C. Hu, Y. Yamauchi, Electric double-layer capacitors based on highly graphitized nanoporous carbons derived from ZIF-67, Chem. Eur. J. 20 (2014) 7895–7900.

[33] I. Hussain, S. Sahoo, T. Hussain, M. Ahmad, M.S. Javed, C. Lamiel, S. Gu, T. Kaewmaraya, M.S. Sayed, K. Zhang, Theoretical and experimental investigation of *in situ* grown MOF-derived oriented Zr-Mn-oxide and solution-Free CuO as hybrid electrode for supercapacitors, Adv. Funct. Mater. 33 (2022), 2210002.

[34] I. Hussain, M.Z. Ansari, M. Ahmad, A. Ali, T. Nawaz, T. Hussain, C. Lamiel, M. Sufyan Javed, X. Chen, M. Sajjad, T. Kaewmaraya, K. Khan, K. Zhang, Understanding the diffusion-dominated properties of MOF-derived Ni–Co–Se/C on CuO Scaffold electrode using experimental and first principle study, Adv. Funct. Mater. 33 (2023), 2302888.

[35] X.L. Xu, W.H. Shi, P. Li, S.F. Ye, C.Z. Ye, H.J. Ye, T.M. Lu, A.A. Zheng, J.X. Zhu, L. X. Xu, M.Q. Zhong, X.H. Cao, Facile fabrication of three-dimensional graphene and metal-organic framework composites and their derivatives for flexible all-solid-state supercapacitors, Chem. Mater. 29 (2017) 6058–6065.

[36] H.F. Zhang, X.H. Lu, L. Yang, Y. Hu, M.Y. Yuan, C.L. Wang, Q.R. Liu, F.F. Yue, D. Zhou, Q.H. Xia, Efficient air epoxidation of cycloalkenes over bimetal-organic framework ZnCo-MOF materials, Mol. Catal. 499 (2021), 111300.

[37] X. Song, M. Oh, M.S. Lah, Hybrid bimetallic metal-organic frameworks: modulation of the framework stability and ultralarge CO_2 uptake capacity, Inorg. Chem. 52 (2013) 10869–10876.

[38] L.Y. Chen, H.F. Wang, C.X. Li, Q. Xu, Bimetallic metal-organic frameworks and their derivatives, Chem. Sci. 11 (2020) 5369–5403.

[39] Y.Y. Lu, Y.T. Wang, H.L. Li, Y. Lin, Z.Y. Jiang, Z.X. Xie, Q. Kuang, L.S. Zheng, MOF-derived porous Co/C nanocomposites with excellent electromagnetic wave absorption properties, ACS Appl. Mater. Interfaces 7 (2015) 13604–13611.

[40] L. He, L. Li, L.Y. Zhang, S.X. Xing, T.T. Wang, G.Z. Li, X.T. Wu, Z.M. Su, C.G. Wang, ZIF-8 templated fabrication of rhombic dodecahedron-shaped ZnO@SiO_2, ZIF-8@SiO_2 yolk-shell and SiO_2 hollow nanoparticles, CrystEngComm 16 (2014) 6534–6537.

[41] J.Y. Chen, X. Zhou, M.M. Zhang, J.Y. Wang, H. Li, J.L. Wang, C.R. Wang, Designing of carbon cloth @ Co-MOF @ SiO_2 as superior flexible anode for lithium-ion battery, J. Alloys Compd. 902 (2022), 163680.

[42] G. Kresse, J. Furthmuller, Efficiency of ab-initio total energy calculations for metals and semiconductors using a plane-wave basis set, Comput. Mater. Sci. 6 (1996) 15–50.

[43] G. Kresse, J. Furthmuller, Efficient iterative schemes for ab initio total-energy calculations using a plane-wave basis set, Phys. Rev. B 54 (1996) 11169–11186.

[44] J.P. Perdew, K. Burke, M. Ernzerhof, Generalized gradient approximation made simple, Phys. Rev. Lett. B 77 (1996) 3865–3868.

[45] G. Kresse, D. Joubert, From ultrasoft pseudopotentials to the projector augmented-wave method, Phys. Rev. B 59 (1999) 1758–1775.

[46] P.E. Blochl, Projector augmented-wave method, Phys. Rev. B 50 (1994) 17953–17979.

[47] J. Xu, L. Wang, K.J. Huang, P. Chen, G. li, Z. Dong, L. Fang, Hollow nanorods MoS_2@SnS heterojunction for sodium storage with enhanced cyclic stability, Chem. Eng. Sci. 256 (2022), 117702.

[48] J. Xu, Z. Dong, Y. Li, K.J. Huang, K. Liu, C. Cao, Freestanding wide layer spacing MoS_2@WS_2@CC ternary structure with fast diffusion path for a highly activity zinc-ion batteries, Appl. Surf. Sci. 613 (2023), 156146.

[49] E. Ercarikci, K.D. Kiransan, E. Topcu, Three-dimensional ZnCo-MOF modified graphene sponge: flexible electrode material for symmetric supercapacitor, Energy Fuels 36 (2022) 1735–1745.

[50] S.A. Pawar, D.S. Patil, J.C. Shin, Cadmium selenide microspheres as an electrochemical supercapacitor, Mater. Today Chem. 4 (2017) 164–171.

[51] A.P. Kumar, B.T. Huy, B.P. Kumar, J.H. Kim, V.D. Dao, H.S. Choi, Y.I. Lee, Novel dithiols as capping ligands for CdSe quantum dots: optical properties and solar cell applications, J. Mater. Chem. C 3 (2015) 1957–1964.

[52] Y.Z. Xu, C.Z. Yuan, X.P. Chen, Co-Doped NiSe nanowires on nickel foam via a cation exchange approach as efficient electrocatalyst for enhanced oxygen evolution reaction, RSC Adv. 6 (2016) 106832–106836.

[53] F.J. Kong, J. Wang, Z.S. Han, B. Qian, S. Tao, H.M. Luo, L. Gao, Lithium storage mechanisms of CdSe nanoparticles with carbon modification for advanced lithium ion batteries, Chem. Commun. 55 (2019) 2996–2999.

[54] M. Li, Z.Y. Meng, R.C. Feng, K.L. Zhu, F.F. Zhao, C.R. Wang, J.L. Wang, L.W. Wang, P.K. Chu, Fabrication of bimetallic oxides (MCo_2O_4: M=Cu, Mn) on ordered microchannel electro-conductive plate for high-performance hybrid supercapacitors, Sustainability 13 (2021) 9896.

[55] J. Xu, Z. Dong, K.J. Huang, T. Wang, Y. Qi, Y. Sun, X. Wu, Preparation of large layer spacing bimetallic sulfide hollow nanosphere for high-energy battery system application, Appl. Surf. Sci. 637 (2023), 157959.

[56] M. Li, K.L. Zhu, Z.Y. Meng, R.H. Hu, J.L. Wang, C.R. Wang, P.K. Chu, Efficient coupling of MnO_2/TiN on carbon cloth positive electrode and Fe_2O_3/TiN on carbon cloth negative electrode for flexible ultra-fast hybrid supercapacitors, RSC Adv. 11 (2021) 35726–35736.

[57] C. Tang, R. Zhang, W.B. Lu, L.B. He, X. Jiang, A.M. Asiri, X.P. Sun, Fe-doped CoP nanoarray: a monolithic multifunctional catalyst for highly efficient hydrogen generation, Adv. Mater. 29 (2017), 1602441.

[58] X. Wang, Y.P. He, Z.C. Guo, H. Huang, P.P. Zhang, H.B. Lin, Enhanced electrochemical supercapacitor performance with a three-dimensional porous boron-doped diamond film, New J. Chem. 43 (2019) 18813–18822.

[59] J. Wang, J. Polleux, J. Lim, B. Dunn, Pseudocapacitive contributions to electrochemical energy storage in TiO_2 (anatase) nanoparticles, J. Phys. Chem. C 111 (2007) 14925–14931.

[60] M. Yaseen, M. Dilawar, H. Ambreen, S. Bibi, S.U. Rehman, U. Shahid, M.K. Butt, A. Ghaffar, A. Murtaza, Electronic, optical and magnetic properties of low concentration Ni-doped CdSe by first principle method, Bull. Mater. Sci. 43 (2020) 122.

[61] Y. Liu, J. Xu, K.J. Huang, L. Wang, Z. Dong, Y. Li, Design of Rubik's cube-like hollow bimetallic sulfide nanocomposite for high-energy battery application, J. Power Sources 563 (2023), 232846.

[62] J. Xu, Q. Liu, Z. Dong, L. Wang, X. Xie, Y. Jiang, Z. Wei, Y. Gao, Y. Zhang, K. Huang, Interconnected MoS_2 on 2D graphdiyne for reversible sodium storage, ACS Appl. Mater. Interfaces 13 (2021) 54974–54980.

[63] K.N. Li, K. Zheng, Z.F. Zhang, K. Li, Z.Y. Bian, Q. Xiao, K.J. Zhao, H.Y. Li, H.J. Cao, Z.B. Fang, Y.Y. Zhu, Three-dimensional graphene encapsulated hollow $CoSe_2$-$SnSe_2$ nanoboxes for high performance asymmetric supercapacitors, Nanotechnology 33 (2022), 165602.

[64] Y.Q. Kuai, T.L. Wang, M.T. Liu, H.W. Ma, C.J. Zhang, Flower-like $Ni_{0.85}Se$ nanosheets with enhanced performance toward hybrid supercapacitor, Electrochim. Acta 321 (2019), 134701.

[65] Y.R. Zhu, X.H. Chen, H. Chen, X.B. Ji, Y. Liu, 3D nanosheet-assembled CoSe Quasi-microspheres as advanced electrode materials for electrochemical energy storage, J. Electrochem. Soc. 164 (2017) A2341–A2347.

[66] S. Majumder, S. Karade, R. Kumar, M.J. Gu, B.R. Sankapal, K.H. Kim, PbS nanoparticles anchored 1D-CdSe nanowires: core-shell design towards energy storage supercapacitor application, J. Alloys Compd. 906 (2022) 164323.

[67] P. Liu, J. Han, K. Zhu, Z. Dong, L. Jiao, Heterostructure $SnSe_2$/ZnSe@PDA nanobox for stable and highly efficient sodium-ion storage, Adv. Energy Mater. 10 (2020), 2000741.

Supporting Information

CdSe-Nanoparticles-Regulated Synthesis of ZnCo-MOFs Derived Conductive Porous Carbon Nanoflakes on Carbon Cloth for Flexible Sodium-Ion Supercapacitors

Hanxue Zhao[a], Mai Li[a*], Jintao Du[a], Yuhang Lei[a], Ayesha Irfan[a], Muhammad Imran[a], Chunrui Wang[a], Jun Yu[b], Jun He[b], Paul K. Chu[c]

[a] College of Science, Donghua University, Shanghai 201620, China

[b] Semiconductor New Materials Research and Development Center, SHANGHAI Q-TECH CO., LTD., Zhengxue Road, Yangpu District, Shanghai, China

[c] Department of Physics, Department of Materials Science and Engineering, Department of Biomedical Engineering, City University of Hong Kong, Tat Chee Avenue, Kowloon, Hong Kong, China

* Corresponding author: E-mail: limai@dhu.edu.cn (M. Li)

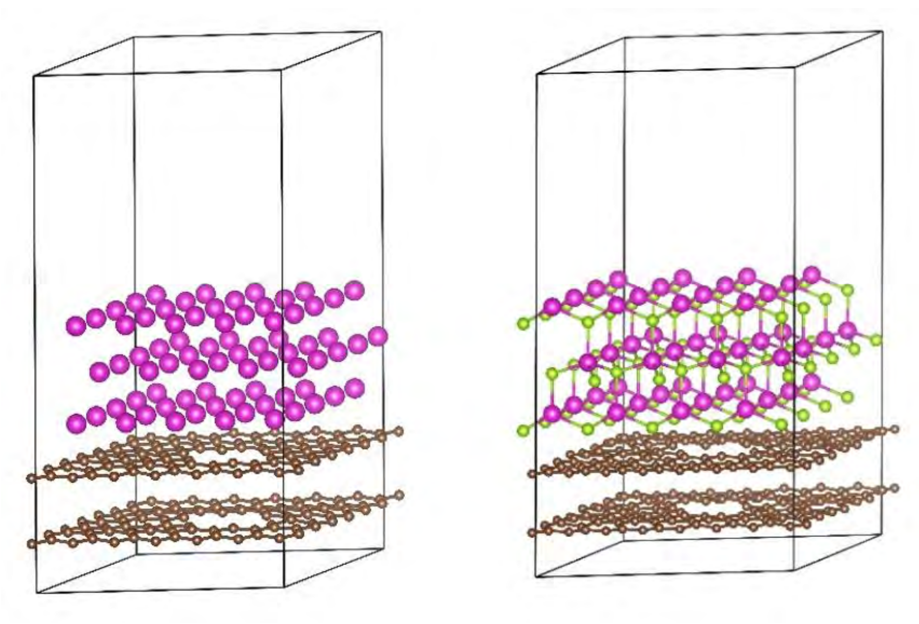

Fig. S1. Structural models of Cd/CPCN@CC and CdSe/CPCN@CC.

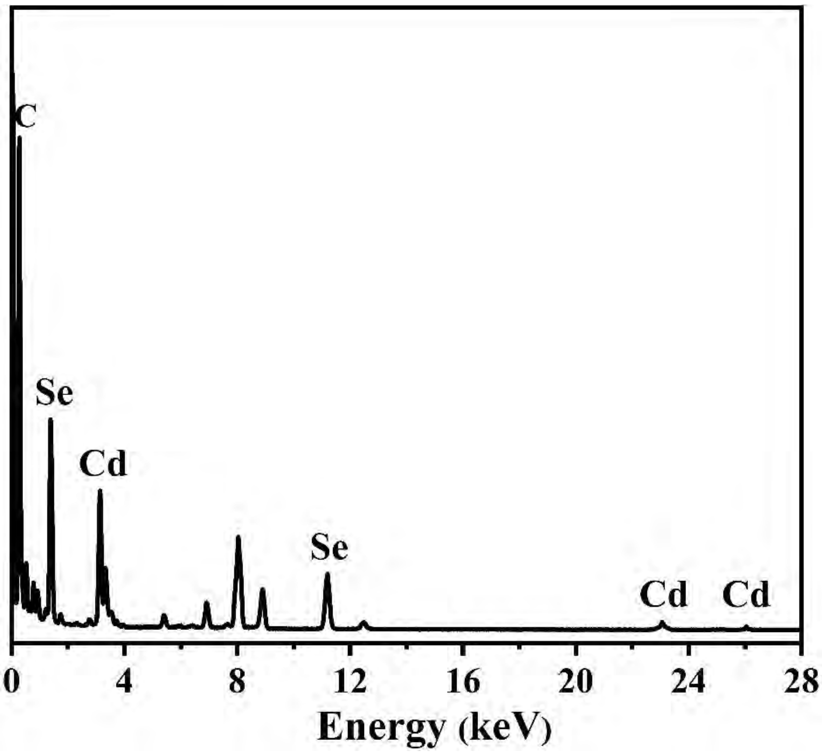

Fig. S2. EDS Survey spectrum of CdSe/CPCN@CC.

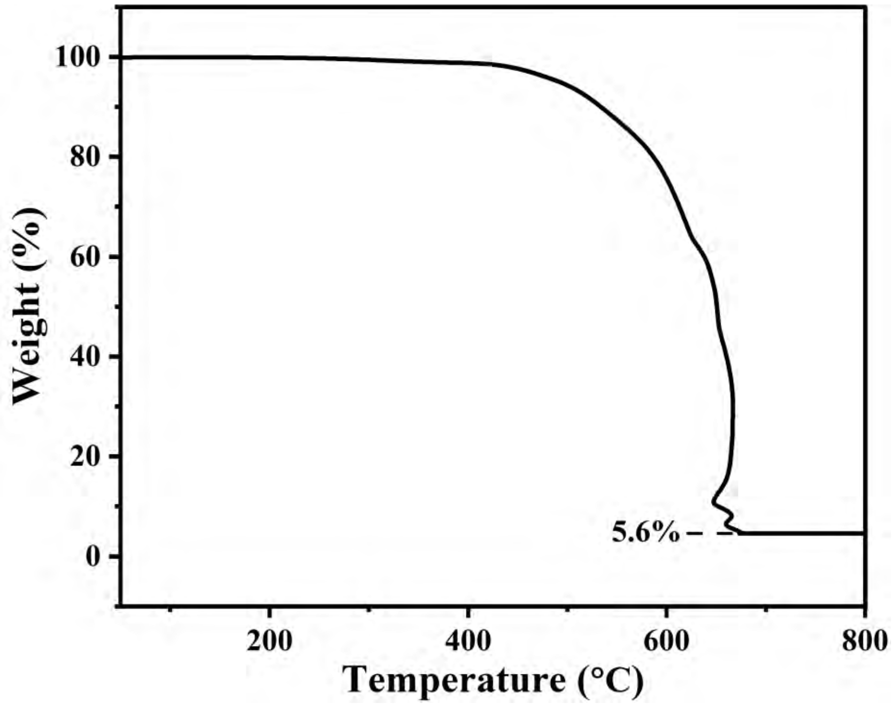

Fig. S3. TGA curve of CdSe/CPCN@CC.

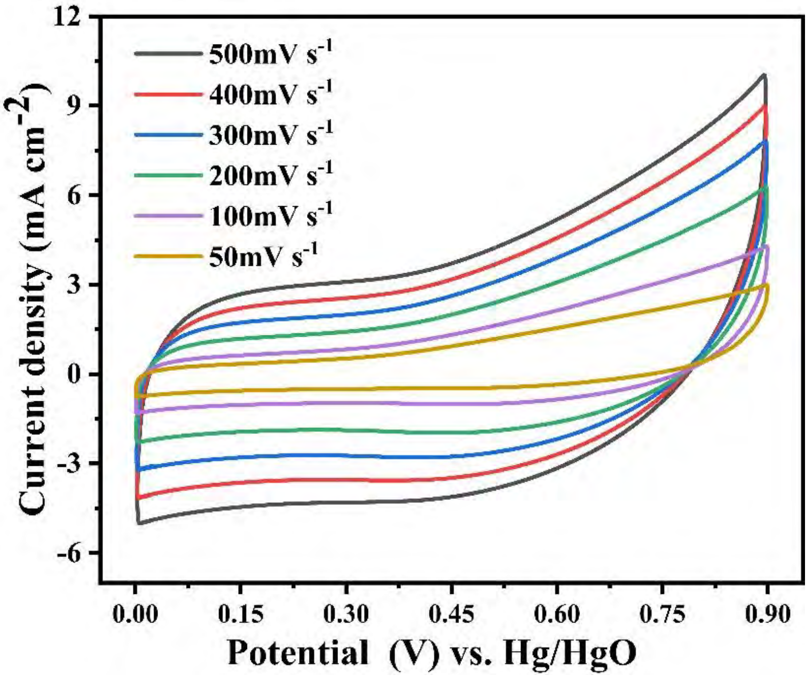

Fig. S4. CV curves of Cd/CPCN@CC.

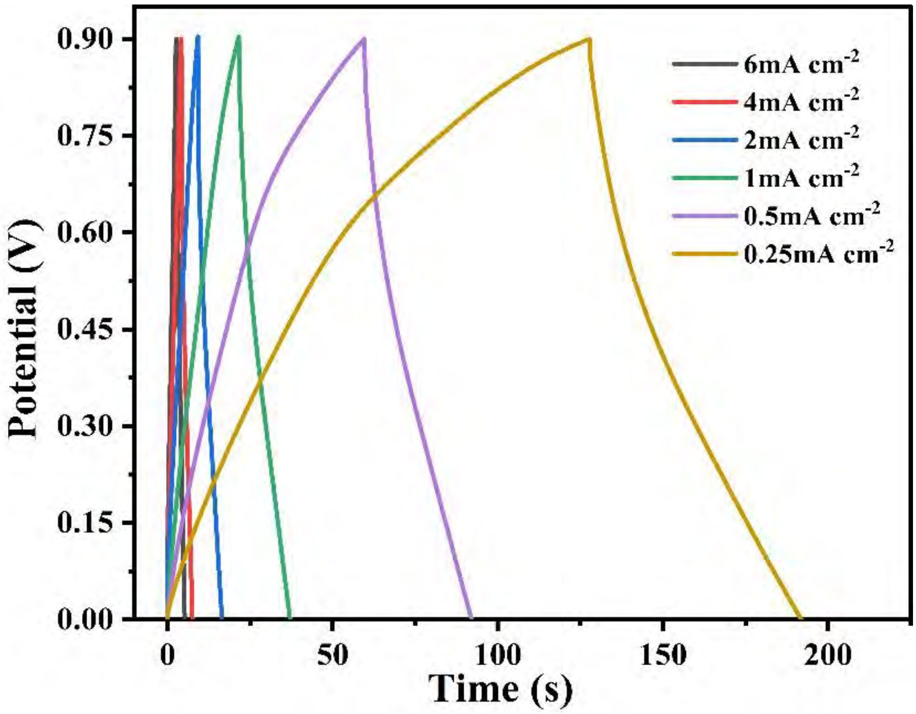

Fig. S5. GCD curves of Cd/CPCN@CC.

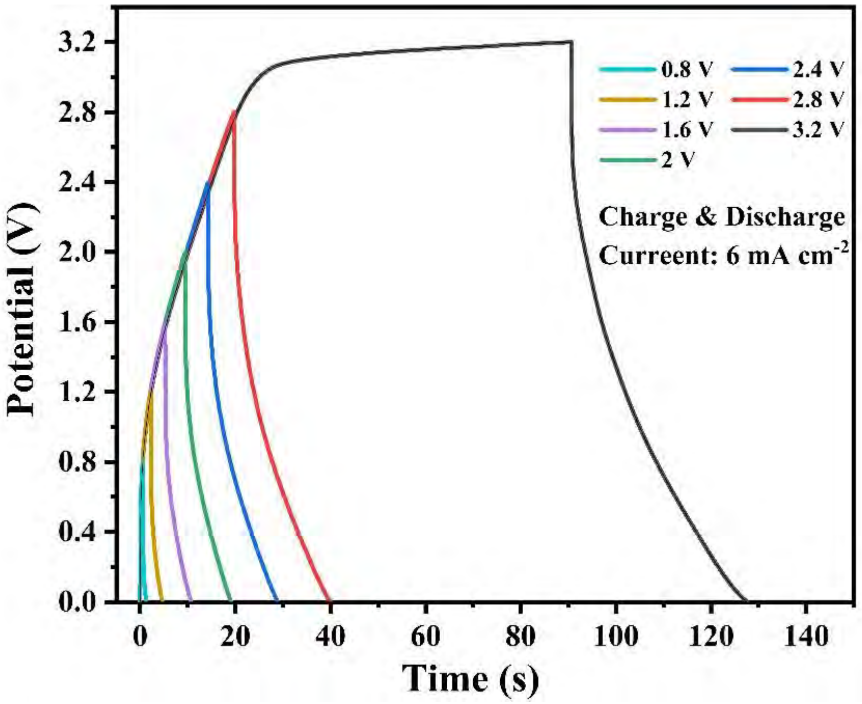

Fig. S6. GCD curves of AC//Cd/CPCN@CC at 6 mA cm^{-2} with different upper cut-off voltages.

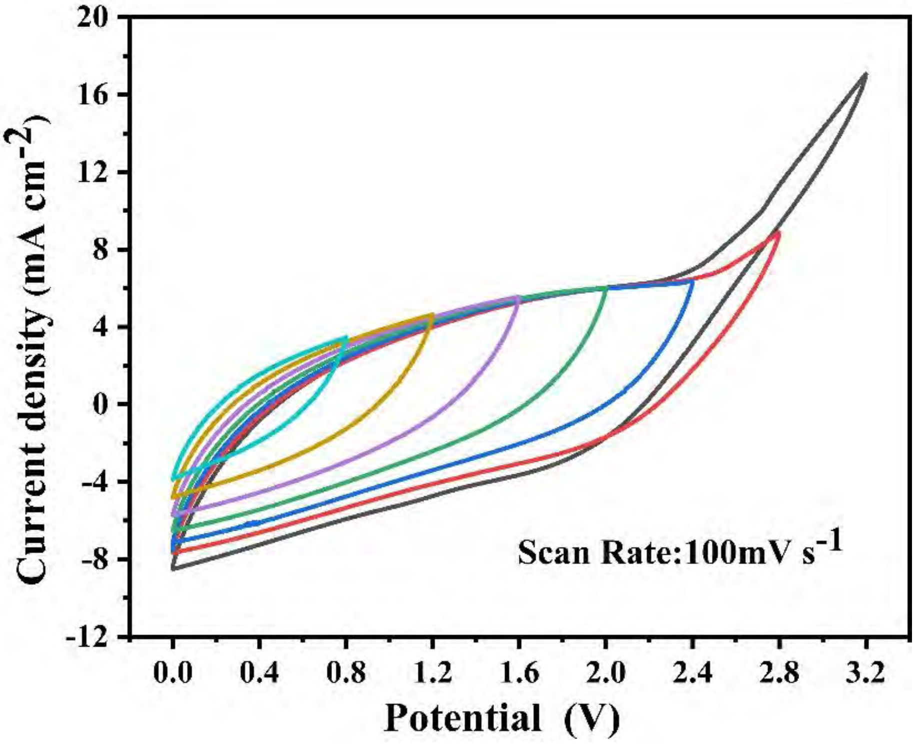

Fig. S7. CV curves of AC//Cd/CPCN@CC at 100 mV s^{-1} with different upper cut-off voltages

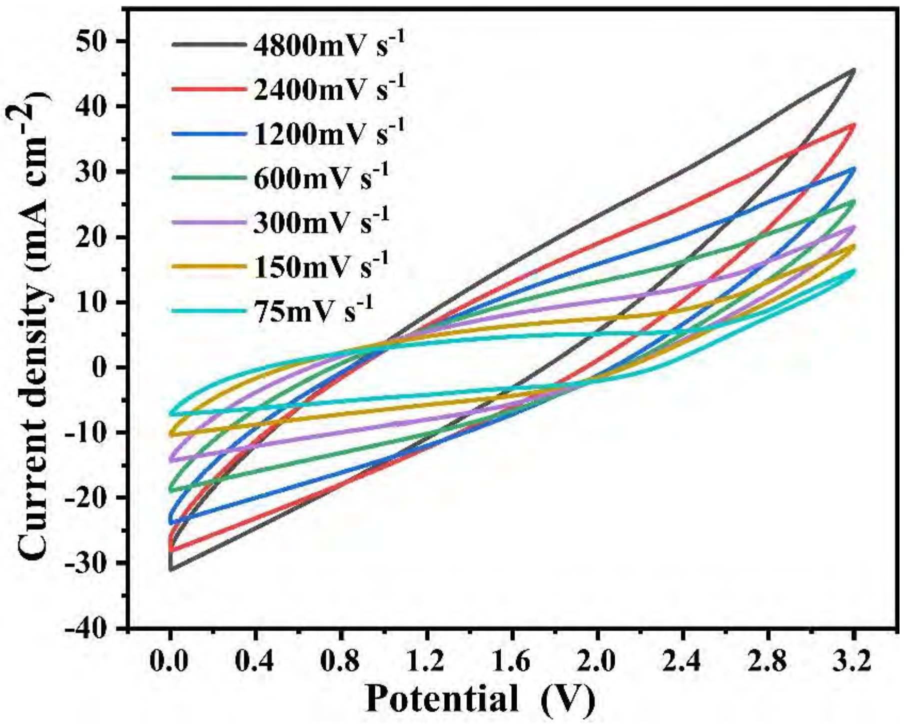

Fig. S8. CV curves of AC//Cd/CPCN@CC.

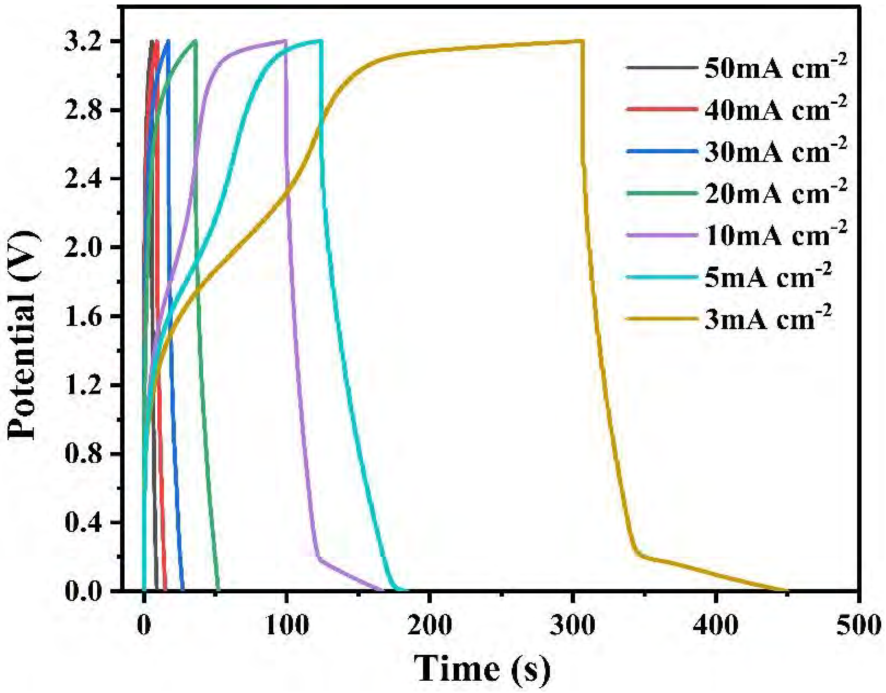

Fig. S9. GCD curves of AC//Cd/CPCN@CC.

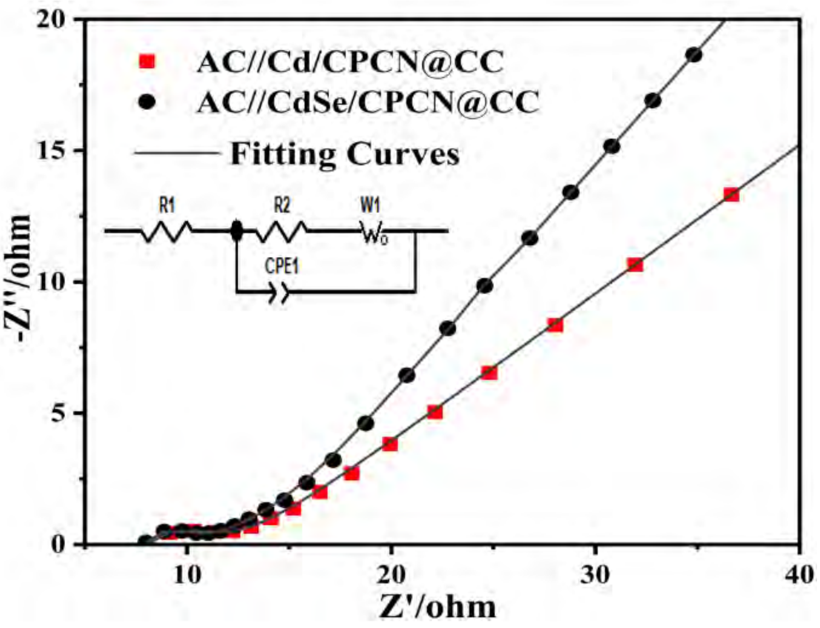

Fig. S10. Nyquist plots curves of AC//CdSe/CPCN@CC and AC//Cd/CPCN@CC.

Table S1. Specific capacitances, energy densities, and power densities of AC//CdSe/CPCN@CC under different current densities.

Electrodes	**Current Density ($mA\ cm^{-2}$)**	**Specific Capacitance ($F\ g^{-1}$)**	**Energy Density ($Wh\ kg^{-1}$)**	**Power Density ($Wh\ kg^{-1}$)**
AC//CdSe/CPCN@CC	1	97.80	139.10	589.82
AC//CdSe/CPCN@CC	2	75.33	107.14	1179.48
AC//CdSe/CPCN@CC	3	66.42	94.47	1769.36
AC//CdSe/CPCN@CC	4	62.30	88.61	2359.44
AC//Cd/CPCN@CC	4	17.25	24.53	2264.31
AC//CdSe/CPCN@CC	5	58.05	82.56	2948.57
AC//CdSe/CPCN@CC	6	56.31	75.86	3748.96
AC//CdSe/CPCN@CC	7	50.88	72.36	4128.31